CHAPTER 3 Self-organization of drops in 2D microchannels

3.1 PRELUDE

A 2D microchannel is a channel with a Hele-Shaw type geometry which sandwiches drops between the upper and lower walls, allowing the drop to move only in the available 2D space. When drops flow in a 2D channel they can approach each other and interact hydrodynamically to form complex spatio-temporal patterns. The governing equations for fluid flow in microchannels is linear due to the creeping flow approximation ($N_{RE} \ll 1$). However, particle motion in the flow field, in the Lagrangian description, can be expressed by $\dot{x} = v(x,t)$ where v is non-linear in space and time. This makes the particle motion problem a non-linear problem which in several instances, has exhibited chaos[6,119]. When drops are involved, non-linearity arises due to two reasons: first is the non-linear velocity field of the continuous phase that will result in the motion of the drops inside the microchannel, and the second reason is coupling of the motion between the drop and the continuous phase. Drops in a 2D microchannel can interact to form ordered arrangements as observed by Jose and Cubaud[53] or disordered ensemble as observed by Beatus and co-workers[40,41]. When the drops are constrained by the upper and lower walls, there can be two configurations depending on the level of confinement. Drops can either retain their spherical shape when the depth of the channel (d) is greater than or equal to the radius of the drop as in the case of Jose and Cubaud[53] ($2R \leq d$), or squished like a pan-cake as observed by Beatus and co-workers in their experiments[53] where the channel depth was smaller than the radius of the drop ($2R > d$). The behavior of drops can be very different for the two cases. For the case where $2R > d$, drops are slowed down by the friction with

the top and bottom walls generating disturbance fields which have dipole-like functional form, exhibiting long range interactions[40,120]. This dipole force affects the drop motion and pattern formation resulting in a disordered ensemble as drops move in the channel. The nature of the dipole force results in a range of interesting collective behaviors like coupling of drops, dynamic assembly and disassembly, phonon-like disturbance propagation, Burger's shock wave etc. in quasi-1D and 2D microchannel systems.

When $2R \leq d$, the drops move with a velocity faster than or very close to the superficial velocity of the continuous phase. As a result, the long range dipole forces are absent. In this chapter, we investigate the drop-pattern formation in 2D microchannels for operating regimes where, $2R \leq d$. Drops hydrodynamically interact to form ordered 2D arrangements. We study the dynamic pattern formation problem and propose models to relate the drop motion to the operation and geometry of the microchannel. The idea is to establish a direct connection between the patterns formed and the operating and design parameters so that the models can eventually be incorporated into design routines to identify methods to design and operate microchannels to arrive at spatio-temporal patterns of interest.

3.2 AGENT BASED FRAMEWORK

In an agent based approach to modeling drop motion, drops (agents) are modeled as point objects moving in the microchannel. They are assumed to be non-deformable which is typically the case when the capillary number associated with the flow is very low (surface tension dominates over viscous forces). The motion of drops is constrained to 2D which allows us to represent drops as circles. The analysis is restricted to cases where the drops do not coalesce- e.g. an incubator device under stable operation. Coalescence can be prevented by generous addition of surfactants to stabilize the emulsion[9]. But adding surfactant in excess would also increase the deformability of the drop. Instead one can employ a highly viscous continuous phase which increases the time required for the thin film between the drops to drain when they approach each other[53]. When drops reside in a 2D microchannel for a time less than this drainage time, coalescence can be prevented. In this framework, it is also possible to model deformable drops while only accounting for the point mass of the drop, by capturing the anisotropic nature of the interaction that arises due to the deformation of the drop.

In this chapter we propose the 'interacting drop traffic models' to identify and model the different forces on the drops as they move in the 2D microchannel. The modeling exercise is restricted to systems which have a top-down symmetry- simplifying the description of the direction of continuous phase flow in the channel needed to compute the various drop-interactions. Once the different forces are quantified, the position and velocity of the drops can be estimated by solving the Newton's second law of motion, as shown in Eq(3-1), for all the drops simultaneously.

$$M_i \frac{d\vec{U}_i}{dt} = \sum \vec{F}_i \tag{3-1}$$

3.2.1 Interacting drop-traffic models

Interacting drop-traffic models provide a simple description for the different forces acting on the drop as it travels inside the microchannel. For the case of a single drop moving inside the channel, far away from the walls, the only force it experiences is the *drag force due to the flow of the continuous phase* around the drop. This interaction is a result of the pressure driven flow that forces the drop to move. Inspired by the solution to the classic problem of fluid flow past a sphere, at low Reynolds number, the x-component of the force is assumed to be proportional to the relative velocity between the drop and the continuous phase[67]. The first term of the RHS of Eq (3-2) explains the relative velocity between the drop and the local average continuous phase velocity. One can also look at the x component force as a superposition of the forcing due to the flow of the continuous phase $k_f\big(\langle v_{A,i}\rangle + \langle v_{B,i}\rangle\big)/2$ and the damping force on the drop due to its movement in the viscous continuous phase $-k_f \beta U_{i,x}$. [Note: in this section we use v to represent continuous phase velocity and U to represent drop phase velocity].

Depending on the lateral position of the drop (y-position: assuming that the axis of symmetry of the channel is oriented along the x-axis), the total resistance offered for the flow for both the continuous and the drop phase varies[67]. The configuration where the drop is at the line of symmetry (x-axis) results in the least resistance for flow, which can be determined by calculating the pressure drop as a function of the y-position of the drop. When the drop is at this position the average velocities on either side of the drop in the y-direction (above and below the drop) are the same because of the top-down symmetry of the microchannel. The y-component force on the drop acts in the direction that will reduce the difference in the velocities above and below the drop, locally ensuring least resistance

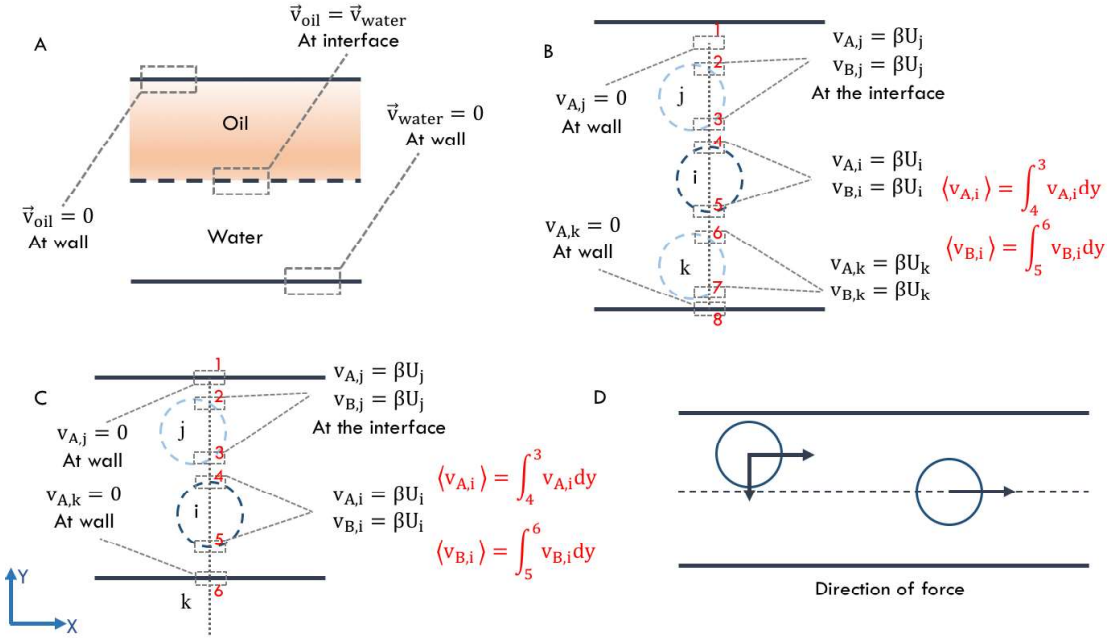

Figure 3-1 A) The velocity boundary conditions for a simple two phase flow system: stratified flow of two fluids bounded by rigid walls[67]; B) Boundary conditions to determine $v_{A,i}$ and $v_{B,i}$ for drop i: the average continuous phase velocity is determined by integrating $v_{A,i}$ over drop interfaces 4 and 3 and $v_{B,i}$ over 5 and 6; C) Boundary conditions to determine $v_{A,i}$ and $v_{B,i}$ for drop i: the average continuous phase velocity is determined by integrating $v_{A,i}$ over drop interfaces 4 and 3 and $v_{B,i}$ between drop interface 5 and wall 6; D) Direction of force on the drops as a function of its position laterally.

for flow around the drop. Hence it takes the form $k_f k'\left(\langle v_{A,i}\rangle - \langle v_{B,i}\rangle\right)$. The damping force on the drop due to its motion in the viscous continuous phase is $-k_f \beta U_{i,y}$. The superposition of the two, results in $k_f k'\left(\langle v_{A,i}\rangle - \langle v_{B,i}\rangle\right) - k_f \beta U_{i,y}$ as explained by the second term in Eq (3-2). If $\langle v_{A,i}\rangle$ and $\langle v_{B,i}\rangle$ are the average velocities of continuous phase above and below drop i, which has a velocity $\vec{U}_i = U_{i,x}\hat{e}_x + U_{i,y}\hat{e}_y$, then the force due to flow of continuous phase $\vec{F}_{f,i}$ is characterized by Eq (3-2) where β is the ratio of the velocity of continuous phase at the drop-continuous phase interface to the translational velocity of the drop.

$$\vec{F}_{f,i} = k_f \left[\frac{\left(\langle v_{A,i}\rangle + \langle v_{B,i}\rangle\right)}{2} - \beta U_{i,x}\right]\hat{e}_x + k_f\left[k'\left(\langle v_{A,i}\rangle - \langle v_{B,i}\rangle\right) - \beta U_{i,y}\right]\hat{e}_y \qquad (3\text{-}2)$$

Knowledge of the approximate velocity profiles of the continuous phase fluid above and below the drop $v_{A,i}$ and $v_{B,i}$ respectively is essential to estimate the force on the drops. Similar to the solution to the pressure driven flow through infinite parallel plates, we assume a parabolic flow profile above and below the drop as shown in Eq (3-3) (chapter 3

in Leal[67]). The term A_i in Eq (3-3) is kept the same for a given cross-section because it approximately characterizes the pressure gradient due to the resistance offered for the flow. One should note that A_i will be minimum when the drop is at the center, in the single drop case.

$$v_{A,i} = A_i y^2 + B_{i,A} y + C_{i,A}$$
$$v_{B,i} = A_i y^2 + B_{i,B} y + C_{i,B} \quad (3\text{-}3)$$

When only one drop is present in the microchannel at a given area of cross-section, $v_{a,i}$ represents the velocity profile of the continuous phase bounded by the top wall and drop boundary and $v_{b,i}$ represents the velocity profile bounded by the drop boundary and the bottom wall. If there is a drop above and/or below the selected drop as illustrated in Figure 3-1 B and C, then $v_{a,i}$represents the velocity profile of continuous phase bounded by drop i and drop j and $v_{b,i}$ represents the velocity profile bounded by the drop boundary and drop k or the bottom wall. The constants in Eq (3-3) can be calculated using the boundary conditions for velocity that should be satisfied. Figure 3-1 A illustrates these conditions on velocity, for a simple case of stratified flow in a microchannel (chapter 2 in Leal[67]). The velocity of the fluids is equal to zero at the boundary (wall), which is commonly referred to as the no-slip condition. At the fluid interfaces, the velocity in the direction normal to the interface should be equal for both fluids, on either side of the interface, to satisfy the mass conservation, that is the kinematic condition. The tangential boundary condition for velocity however, does not have a sound physical basis as the normal velocity. Common practice it to adopt a continuity condition across the interface (phenomenological in nature); dynamic boundary condition which has worked well for a reasonable range of problems. Then the final condition on the velocities is mass conservation. The velocities integrated over the area of cross-section, should be equal to the total flowrate of the fluids.

For a single drop traveling along the axis of symmetry of the microchannel, the only force acting on the drop would be the x-component of the force due to the flow of the continuous phase F_f which results in drop velocity as explained by Eq (3-4).

$$U_{i,x} = \frac{1}{\beta} \frac{\left(\langle v_{a,i} \rangle + \langle v_{b,i} \rangle\right)}{2} \quad (3\text{-}4)$$

Experimentally it has been observed by Jose and Cubaud[53] that the velocity of the drop is proportional to the superficial velocity of the fluid in the 1-D geometry. In the network model, this information is explicitly used while calculating the velocity of the drops[97,99]. Sessoms et al. (2009) considered the effects of pressure drop on the continuous phase and drop phase separately and estimated the velocity of the drop as a multiple of the superficial velocity. In the drop-traffic models we consider internal circulations inside the drop, by stating that the velocity of the continuous phase at the drop-fluid interface is βU_d. In Eq (3-4) $\langle v_{a,i} \rangle$ and $\langle v_{b,i} \rangle$ are functions of U_i. With boundary conditions and mass conservation, it is possible to express the constants in Eq. (3-3) analytically to get an expression for the velocity of the drop U_i. On simplification, we get Eq (3-5) where d represents the depth in the direction perpendicular to the 2D flow area and H represents the width of the channel in the y direction (perpendicular to the longitudinal direction). Expanding the RHS of Eq (3-5) about $(\beta - 1)$, we see that the velocity is proportional to the superficial velocity. In a 2-D microchannel, the large cross section, presence of other drops and the complex flow fields complicate the determination of β associated with the drop.

$$U_{i,x} = \frac{Q_t}{d(2R(1-\beta) + \beta H)}$$
$$U_{i,x} = \left(\frac{Q_t}{2RH}\right)\left[1 + \frac{(H-R)(\beta-1)}{H} + \frac{(H-R)^2(\beta-1)^2}{H^2} + O(\beta-1)^3\right] \quad (3\text{-}5)$$

The continuous phase flow around the drops, forces them to move in the channel. The geometry of the channel dictates the magnitude of this force $\vec{F}_{f,i}$ on the drop. Depending on whether the 2D microchannel diverges or converges, drops can either slow down or speed up in the channel as a result of the mass conservation- which has been incorporated in the calculation of the average velocities around the drops. Hence based on the position of drops and the channel geometry, drops can experience different magnitudes of force F_f^i which would facilitate relative motion between drops. When two drops approach each other the viscous continuous phase between them is drained. As the distance between the drops reduces, the drainage of the viscous fluid generates larger pressure fields due to the fluid motion in the thin region between the drops. This phenomenon is called the lubrication flow and is illustrated in Figure 3-2. When the distance between the drops reduce with time, the velocity profile of the drainage of fluid becomes steeper as shown in

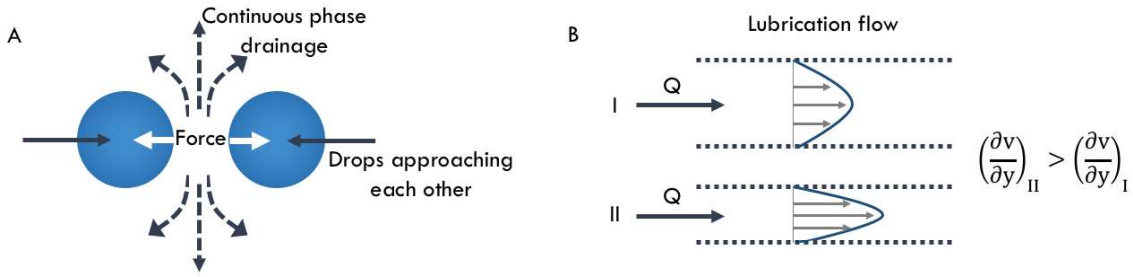

Figure 3-2 A) Two drops approaching each other in a viscous medium drains the fluid between them; B) Drainage flow in the case of approaching drops can be conceptualized as fluid flow between two parallel plates: for a given flowrate Q, the gradient of velocity increases with decrease in the distance between the plates.

Figure 3-2 B. According to the Stokes equation for flow, the pressure forces are balanced by the viscous forces ($\nabla P = \nabla^2 v$). Hence, as the gradient in the velocity increases, the gradient of pressure increases.

This would result in a *force* $\vec{F}_d^{\,i\,j}$ on the drops, which is referred to as the drop-drop interaction, that resists their relative motion as they approach each other as illustrated in Figure 3-2 (A). The functional form for the force for the asymptotic case where there are two drops approaching each other in unbounded flow, can be derived from Stokes equation with the thin film approximation[39]. The expression in Eq (3-6) explains the force between drops in the microchannel where $\vec{d}_{i\,j}$ is the vector pointing form drop 'i' to drop 'j' with k_d and γ as tunable parameters. This drop-drop interaction force due to the lubrication flow is short ranged in contrast to the dipole interactions, that arise in a 2D channel when the drops are pancake like shaped due to confinement, which are long ranged[40]. The denominator term in Eq (3-6) which ensures that the drops never touch each other by allowing $\vec{F}_d^{i,j} \to \infty$ at the limit $\left(\|\vec{d}_{i,j}\| - 2R\right) \to 0$. Hence coalescence cannot be simulated using the interaction term as explained in Eq (3-6). One has to provide additional conditions, like say a critical distance, beyond which the nature of interaction is attractive which pulls the drops together allowing them to attain a different configuration.

$$\vec{F}_d^{i,j} = \begin{cases} \dfrac{k_d \dot{d}_{i,j}}{\|\vec{d}_{i,j}\| - 2R}\,\hat{d}_{j,i} & \|d_{i,j}\| < \gamma R \\ 0 & else \end{cases} \qquad (3\text{-}6)$$

$$\text{where, } \vec{d}_{i,j} = \vec{U}_i.\hat{d}_{i,j} + \vec{U}_j.\hat{d}_{j,i}$$

When a drop approaches a wall, it does not penetrate the wall. This is because of there is a *Force on the drop due to the boundary* $\vec{F}_b^{\,i\,b}$, which is a result of the lubrication flow of

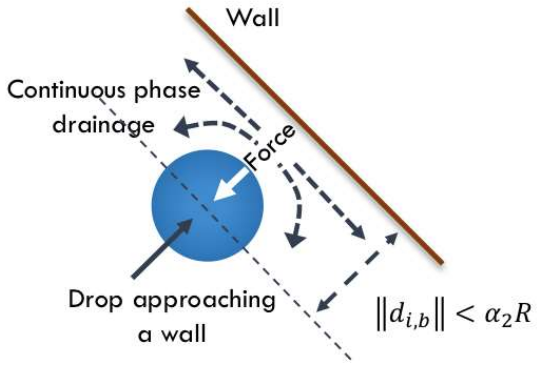

Figure 3-3 Drop approaching a wall (boundary) which results in lubrication flow that generates large pressures. The force on the drop acts in a direction along the line joining the center of the drop to the closest point in the boundary.

the viscous continuous phase between the drop and the wall, that resists the approach. This force is computed by an expression as shown in Eq (3-7), where α_1 and k_b are tuning parameters, which has a functional form similar to Eq (3-6). In Eq (3-7), $\vec{\ }_{i\,b}$ is the vector connecting the drop, to the closest point on the boundary. Drops flowing parallel to the wall experience no force due to the wall because the rate at which they approach it $\dot{\ }_{i\,b}$ goes to zero. Because the drops experience a force only when they are very close to each other or the wall, the effect of these forces are neglected when they are farther than $\alpha_1 R$.

$$\vec{F}_b^{i,b} = \begin{cases} \dfrac{k_b \dot{b}_{i,b}}{\|\vec{b}_{i,b}\| - 2R}\, \hat{b}_{b,i} & \|\vec{b}_{i,b}\| < \alpha_1 R \\ 0 & else \end{cases} \qquad (3\text{-}7)$$

where, $\vec{b}_{i,b} = \vec{U}_i . \hat{b}_{i,b}$

3.2.2 Scaling analysis

Once the different forces acting on the drops are characterized, one can solve the Newton's second law of motion to estimate the position and velocities of the drops in the microchannel as outlined in section 3.2. One can non-dimensionalize Eq (3-8), to identify the relative importance of each of the terms in the equation. Every variable in the equation is expressed as a product of a non-dimensionalized variable, which is an $o(1)$ term that varies from 0 to $O(1)$, and the corresponding scale as shown in Eq (3-9). Once the scales are substituted into Eq (3-8) the terms collected as shown in Eq (3-10) and (3-11). One will see that the Reynolds number multiplies the terms on the RHS of Eq (3-11), which represent the inertial contribution of the system.

$$m_i \frac{dU_i}{dt} = F_f^i + F_d^{i,j} + F_b^{i,b}$$

$$m_i \frac{d\vec{U}_i}{dt} = \begin{bmatrix} k_f\left(\frac{\left(\langle v_{A,i}\rangle + \langle v_{B,i}\rangle\right)}{2} - \beta U_{i,x}\right) \\ k_f\left(k'\left(\langle v_{A,i}\rangle - \langle v_{B,i}\rangle\right) - \beta U_{i,y}\right) \end{bmatrix} + \frac{k_d \dot{d}_{i,j}}{\left\|\vec{d}_{i,j}\right\| - 2R}\hat{d}_{j,i} + \frac{k_b \dot{b}_{i,b}}{\left\|\vec{b}_{i,b}\right\| - 2R}\hat{b}_{b,i} \tag{3-8}$$

$$Where, k_f \sim 6\pi\mu R; k_d \sim 6\pi\mu R^2; k_b \sim 6\pi\mu R^2$$

Scales for all the variables in Eq (3-8). Variables with a bar over them are $o(1)$ non-dimensionalized.

$$\langle v_{A,i}\rangle = U_s\langle \bar{v}_{A,i}\rangle;\ U_i = U_s\bar{U}_i; \left(\left\|\vec{d}_{i,j}\right\| - 2R\right) = \gamma R\left(\left\|\bar{\vec{d}}_{i,j}\right\| - \frac{2}{\gamma}\right);$$
$$\left(\left\|\vec{b}_{i,b}\right\| - 2R\right) = \alpha R\left(\left\|\bar{\vec{b}}_{i,b}\right\| - \frac{2}{\alpha}\right); t = \bar{t}\frac{R}{U_s} \tag{3-9}$$

Substituting the scales and collecting terms:

$$\frac{4}{3}\pi R^3 \rho \frac{U_s^2}{R}\left[\frac{d\bar{U}}{d\bar{t}}\right] = 6\pi\mu R U_s \left[\begin{bmatrix} k_f\left(\frac{\left(\langle \bar{v}_{A,i}\rangle + \langle \bar{v}_{B,i}\rangle\right)}{2} - \beta\bar{U}_{i,x}\right) \\ k_f\left(k'\left(\langle \bar{v}_{A,i}\rangle - \langle \bar{v}_{B,i}\rangle\right) - \beta\bar{U}_{i,y}\right) \end{bmatrix} + \frac{k_d \dot{\bar{d}}_{i,j}}{\gamma\left(\left\|\bar{\vec{d}}_{i,j}\right\| - \frac{2}{\gamma}\right)}\hat{d}_{j,i} + \frac{k_b \dot{\bar{b}}_{i,b}}{\alpha\left(\left\|\bar{\vec{b}}_{i,b}\right\| - \frac{2}{\alpha}\right)}\hat{b}_{b,i}\right] \tag{3-10}$$

$$\left(\frac{2}{3}N_{Re}\right)\frac{dU_i}{dt} = \bar{F}_f^i + \bar{F}_d^{i,j} + \bar{F}_b^{i,b}$$
$$\text{where } N_{Re} = \left(\frac{\rho U_s R}{\mu}\right) \tag{3-11}$$

The very low Reynolds number (N_{Re}<1) of the system would allow us to simplify the governing equations, where inertial contribution of system can be neglected, resulting in Eq(3-12). This is commonly referred to as the creeping flow approximation.

$$\sum \vec{F}_i = 0 \tag{3-12}$$

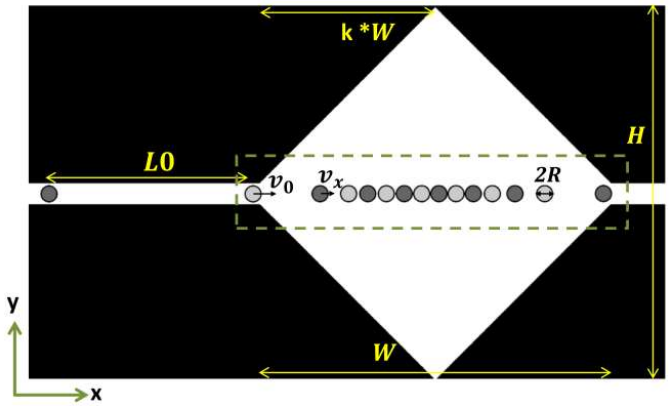

Figure 3-4 Microchannel system chosen for validation of simulation results. Geometry same as [53] [dotted part in the microchannel is where the drop arrangement is seen; k=0.5; W=4.75 mm; H=5 mm; R=0.125 mm.

3.2.3 Algorithm for simulating drop movement

In this section the algorithm for solving the agent based framework, to determine the position and velocities of drops in the microchannel, is presented.

Step 1. Initialize the positions of drops.

Step 2. Compute the velocities of drops that satisfy Eq (3-12).

Step 3. Update positions and go to Step 1.

Evaluating Step 2 requires solving the force balance equations for every drop in the microchannel simultaneously. This would involve solving Eq (3-3), alongside the force balance equations for drops (Eq (3-12)). For the case of a single drop in the microchannel, the unknowns that have to be estimated at any given time instant would be: $A, B_A, C_A, B_B, C_B, U_x, U_y$. The two boundary conditions on the walls, two drop-continuous phase interface conditions, one mass conservation condition, force balance equations in two dimensions. One can clearly see that there are equal number of unknowns and equations, seven in this case. This can be extended to the case of multiple drops where depending on the configuration of drops (number of drops at a given cross section), the number of unknowns vary.

3.3 DYNAMIC PATTERN FORMATION

3.3.1 Microchannel system

To validate the agent based simulations, we compare our results with the experiments of Jose and Cubaud[53]. The microchannel used for the study is a linearly diverging-converging microchannel, with a top-down and fore-aft symmetries as shown in Figure 3-4. The

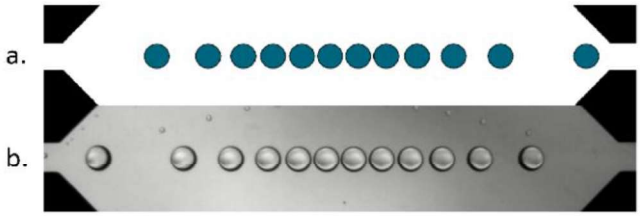

Figure 3-5: One layer configuration: a) Multi agent simulation (>500 ms) $L_0 \sim 38R$; b) Experiments $L_0 \sim 30R$[53]; the microchannel employed is similar to one shown in Figure 3-4 with the image cropped to show only the drop-patterns [video enclosed in CD]

dimensions of the microchannel are chosen to be same as in the experiments of Jose and Cubaud[53] (k=0.5; W=4.75 mm; H=5 mm). When the drops enter the channel at a very small rate, a single layer arrangement is formed inside the microchannel. As the rate of entry of drops increase, the drops acquire a multi-layer conformation. The entry frequency is manipulated in the experiments by controlling the input velocity of drops and the initial spacing between them. However in the experiments of Jose and Cubaud[53], these two manipulated variables were correlated as $L_0/2R = 0.45\ (Q_c/Q_d)$ where L_o is the initial spacing between the drops, R is the radius and Q_c and Q_d are the continuous and discrete phase flow rates, because of the dynamics of the drop-generator. For the purpose of validation, we used the same correlation in our simulations. For the simulation, all the geometrical parameters *k, W, H* and operating parameters v_0, *R,* L_0 [Figure 3-4] are kept the same as the experiments of Jose and Cubaud[53] and the patterns formed are compared.

3.3.2 Tuning the parameters

The phenomenological nature of the forces results in tunable parameters $k_f, k_d, k_b, \alpha_1, \gamma, \beta$ that have to be tuned, to match the experiments quantitatively. From Eq (3-12), because the sum of the forces is zero, one can infer that the ratios of the k's are important and not the absolute values. Tuning is performed to make sure that the simulation was able to predict the different layered configurations for approximately similar operating conditions as in the experiments[53]. The uncertainty in the correlations provided by Jose and Cubaud (2012) that relate the operating conditions (ref section 3.3.1), made the comparison of the experimental data with the simulation results tedious. No rigorous algorithm was followed to tune the models. Constants that accompanied the solution to the asymptotic cases, as explained in section 3.2.1, are retained and the integers multiplying these constants were manipulated to tune the model. Tuning was done based on visual perception. The ease of tuning indicates the robustness of the simulation strategy to changes in the tuning parameters. These tuning parameters are functions of the system properties and geometry.

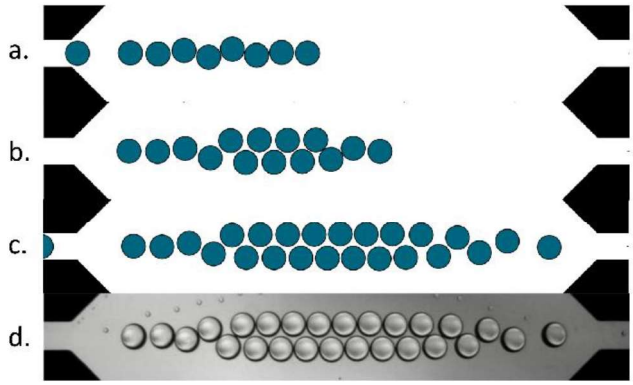

Figure 3-6 Two layer configuration: Multi agent simulation $L_0 \sim 18R$: a-140 ms, b-240 ms, c->500 ms [the drop-drop interaction is zero when drops are not approaching each other]; d.) Experiments $L_0 \sim 14R$[53]; the microchannel employed is similar to one shown in Figure 3-4 with the image cropped to show only the drop-patterns [video enclosed in CD]

Hence, once the tuning parameters are set, only the operating parameters need to be varied to identify the different structures formed inside the microchannel.

3.3.3 One-layer configuration

The drops entering the microchannel decelerate in the diverging section and accelerate in the converging section due to the increasing and decreasing cross-sectional area for flow. The distances between the drops decreases as they slow down and increases as they speed up in the microchannel. As the inlet spacing is reduced, the distance between the drops in the microchannel reduces and they start to interact hydrodynamically as explained by Eq (3-6). For an inlet spacing as large as [redacted] prior to the entry into the microchannel, a single layer of drops is formed as shown in Figure 3-5. One should realize that all the forces, the force on the drop due the flow (F_f) and the hydrodynamic drop-drop interactions (F_d) are constrained to the x direction for the single layer arrangement of drops. Absence of a y-component of force would mean that the drops can never escape the single layer conformation. To capture the effect of the y-component forces, the walls of the microchannel are modified with a very small random roughness factor. This results in a non-zero y-component of F_f [Eq (3-2)] which continuously perturbs the drops from their single layer arrangement, mimicking reality where disturbances are ubiquitous. As the drops start to interact, the y component of the force F_d, between the drops as explained by Eq (3-6) tries to push the drops to the next layer while the y-component of the F_f tries to preserve the single layer configuration. We observed that a competition between the drop-drop interaction forces and the y-component of the force due to flow decided the stability of the single layer arrangement. For a given inlet spacing the simulation was carried out

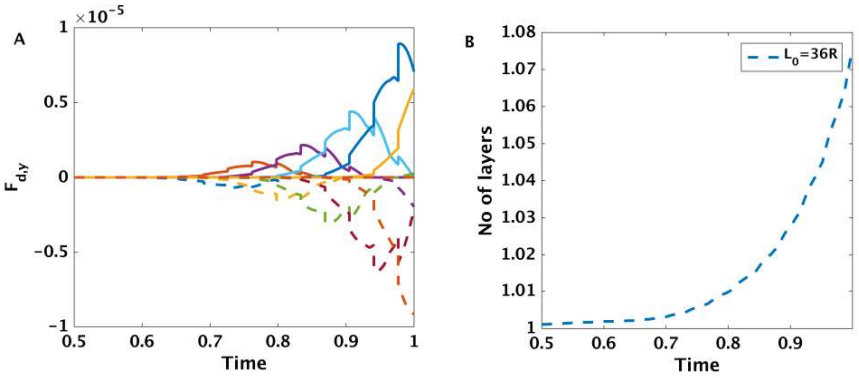

Figure 3-7 A) The y-component of force due to the drop-drop interactions $F_{d,y}$, which is the cause for layering in the system, plotted with time for different drops; B) Time evolution of the number of layers in the system at the onset of instability. Simulations are performed for $L_0 \sim 36\ R$ and (B) contains only the first drops to experience layering.

for different random roughness in the wall. We observed that all the simulations were identical.

3.3.4 Two-layer configuration: The phenomenon of layering

When the initial spacing between the drops is reduced further ($L_0 \leq 36R$), drops start to crowd in the diverging section of the channel. The small disturbance present in the system grows in time because of the drop-drop interactions, resulting in the displacement of a drop from the single layer arrangement. We term this phenomenon as the layering instability, which breaks the top-down symmetry of the single layered arrangement. Figure 3-7 (A) shows the rapid increase in the y-force due to the drop-drop interactions, as drops start to crowd in the channel. This force remains negligible (close to zero) when drops are in a single layer arrangement. Once the 1D drop-assembly is no longer able to house the incoming drops, this force- on the drops- pushes the drop in the y-direction to cause layering in the system. One can observe from Figure 3-7(B: 0.6-0.7 s) that as the y-force increases, number of layers in the channel also increases.

Now the displaced drop is equally likely to move in the positive or the negative y-directions. The random roughness ensures that the probability for displacement of drops is the same for both the directions. Because the drop-drop interactions are directed along the line joining the centers of two drops, the displaced drop upsets its neighbors, and this process continues resulting in a chain reaction that propagates through the drop-train in the microchannel [see Figure 3-6 a], offsetting the drops from their initial arrangement, causing layering. The drops as they come in, arrange themselves in two layers [see Figure 3-6 b]. The steady state patterns look identical for multiple runs of the simulation with different random roughness. The difference is prominent only when we deal with the

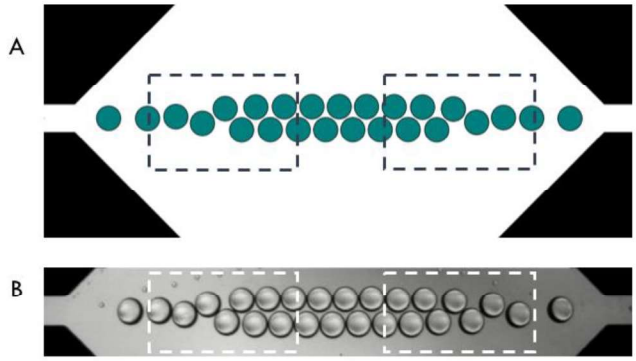

Figure 3-8 A) Multi-agent simulation of two-layer formation with the drop-drop interaction resisting drop retraction in the converging section. This results in a spatial structure with fore-aft symmetry (observe the boxed regions in the figure); B) Experiments of Jose and Cubaud[53] which show the absence of fore-aft symmetry.

motion of a small number of drops, where the choice of the displaced drop to move in the positive and negative directions can yield different results.

We observe, from Figure 3-6 d, that the dynamics in the channel also breaks the fore-aft symmetry of the assembly. In our simulations to capture this effect, we had to neglect the force between drops when the drops are retracting which changes Eq (3-6) to Eq (3-13) with an additional condition $\dot{d}_{i,j} > 0$. Figure 3-8 (A) shows the pattern formation when the drop-drop interaction term used in the multi-agent simulation is given by Eq (3-6).

$$\vec{F}_d^{i,j} = \begin{cases} \dfrac{k_d \dot{d}_{i,j}}{\|\vec{d}_{i,j}\| - 2R}\, \hat{d}_{j,i} & \|d_{i,j}\| < \gamma R, \dot{d}_{i,j} > 0 \\ 0 & else \end{cases} \qquad (3\text{-}13)$$

$$\text{where, } \vec{d}_{i,j} = \vec{U}_i . \hat{d}_{i,j} + \vec{U}_j . \hat{d}_{j,i}$$

This results in an arrangement which preserves its fore-aft symmetry during the dynamic pattern formation. This is contrary to what is observed by Jose and Cubaud in their experiments [Figure 3-8 (B)]. We observe that the force that resists retraction of drops because of the generation of low pressure zone between the drops is cancelled out by other forces which are currently unknown. This could be the reason why, neglecting the force during the retraction of drops allows us to capture the pattern formation in great detail as shown in Figure 3-6 c.

In the converging section of the channel, the accelerating velocity field pulls the drops from the layered structure to form a single layer before exiting the channel [see converging section in Figure 3-6 c], because the size of the exit channel is of the same order of

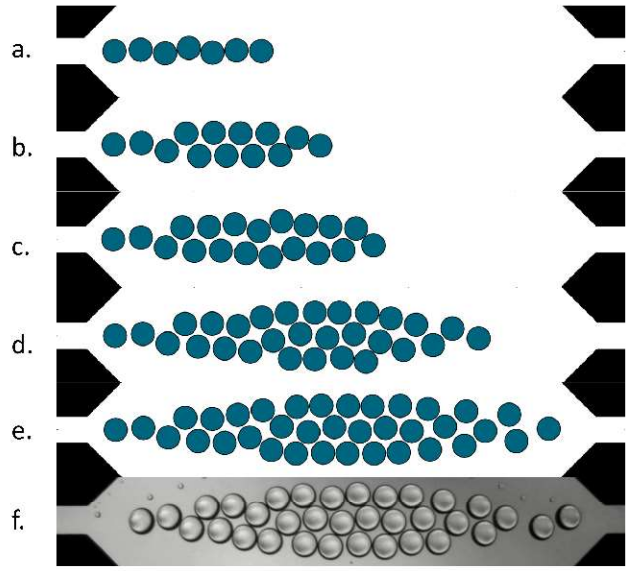

Figure 3-9 (Enhanced online) Three layer configuration: Multi agent simulation $L_0 \sim 12R$: a-75 ms, b-140 ms, c-207 ms, d-320 ms, e->500 ms [the modified drop-boundary interaction was used as given in Eq (3-14)]; f.) Experiments $L_0 \sim 12R$[53] [Enhanced online] [video enclosed in CD]

magnitude of the size of the drop (2R). The asymmetry in the drop-drop interaction force allows us to capture this feature in the dynamic pattern formation.

Beatus and co-workers observe transverse motion of drops from a steady 1D assembly in their experiments which, they refer to as the zigzag instability. Although this transverse movement qualitatively appears similar to the layering instability, the forces that result in the motion have very different origins. The zig-zag instability is a result of the asymmetry in the dipole-like interactions between the drops in the microfluidic crystal near the channel entrance[40], while the layering instability is a result of the lubrication interaction at the diverging section due to the crowding of drops.

3.3.5 Three-layer configuration

For even lower initial spacing of drops ($L_0 < 16R$), the single layer of drops initially formed, becomes unstable [Figure 3-9 a] as explained in the previous section and the drops temporarily assume a two-layer arrangement [Figure 3-9 b]. Unable to house the entering drops, the two-layer arrangement eventually becomes unstable [Figure 3-9 c] and the system drifts away to the next configuration where there are three layers of drops [Figure 3-9 d, e]. The breaking of the two-layer arrangement is similar to that of the one-layer arrangement where the drop that moves away from the layered structure, perturbs all of its neighbor drops destabilizing both the layers. When the three layered assembly approaches the converging section, the drops are pulled away from the assembly before the drops exit.

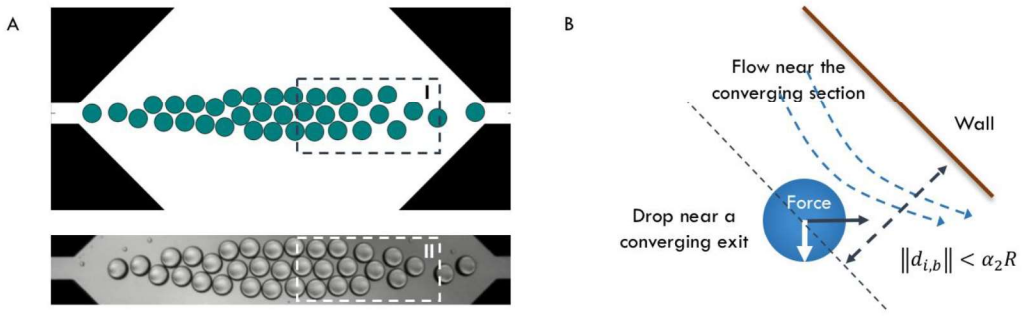

Figure 3-10 (A) Dynamic pattern formation without the additional y-force as explained in (B), compared to experiments of Jose and Cubaud[53]; (B) The additional y-force that captures the exiting of drops is added by modifying the drop-boundary interaction suitably.

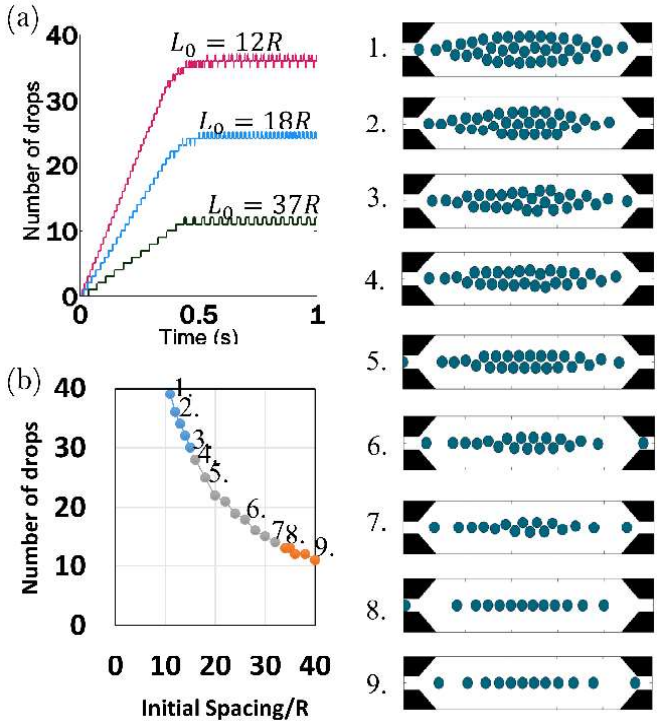

Figure 3-11 a) Time evolution of the number of drops in the microchannel for initial spacing that give one, two and three layers; b) A plot of the number of drops inside a microchannel as a function of the initial spacing between the drops prior to entry into the channel, along with the snapshots of the steady state patterns formed by the drops.

But to make sure that the drops converged to the exit channel, it was necessary to consider an additional y-force on the drops near the converging section of the channel. The drop-boundary interaction was modified, as shown in Eq (3-14), to provide this additional y-force on the drops. In the converging section of the channel the drop structure breaks down in a complex manner to form a single layer of drops before exit. The multi-agent simulation was able to capture these fine qualitative details seen in the experimental videos like the zigzag nature of the middle layer of drops in the three-layer conformation [Figure 3-9 e

and f]. For even smaller inlet spacing (L_0<11R) multiple layers (>3) are observed. This was possible only after the drop-boundary interaction was modified as in Eq (3-14). The values of the tuning parameters used in our simulations are summarized in Table 2.

$$\vec{F}_b^{i,b} = \begin{cases} \dfrac{k_b \dot{b}_{i,b}}{\left\|\vec{b}_{i,b}\right\| - R} \hat{b}_{b,i} & \left\|\vec{b}_{i,b}\right\| < \alpha_1 R;\ \dot{b}_{i,b} > 0 \\ \left(\dfrac{k_b \dot{b}_{i,b}\left(\hat{b}_{i,b}.\hat{e}_y\right)}{\left\|\vec{b}_{i,b}\right\| - R}\right)\hat{e}_y & \alpha_1 R < \left\|\vec{b}_{i,b}\right\| < \alpha_2 R;\ \dot{b}_{i,b} > 0 \\ 0 & else \end{cases} \quad (3\text{-}14)$$

$$\text{where, } \vec{b}_{i,b} = \vec{U}_i.\hat{b}_{i,b}$$

As the drops enter the microchannel, they start to form a dynamic structure. The number of drops inside the microchannel increases steadily till the drop front reaches the exit of the diverging converging microchannel. The number of drops inside the channel stabilizes and a steady dynamic structure is formed [Figure 3-11 a]. This is because the rate at which the drops exit is equal to the rate at which they enter. As the initial spacing is reduced, larger structures are formed and so the number of drops inside the channel also increases [Figure 3-11 b].

Table 2: Tuned parameters	
k_f	$6\pi\mu R$
k_d	$3\times6\pi\mu R^2$
k_b	$5\times6\pi\mu R^2$
γ	2.4R
β	1
α_1	2.4 R
α_2	10 R

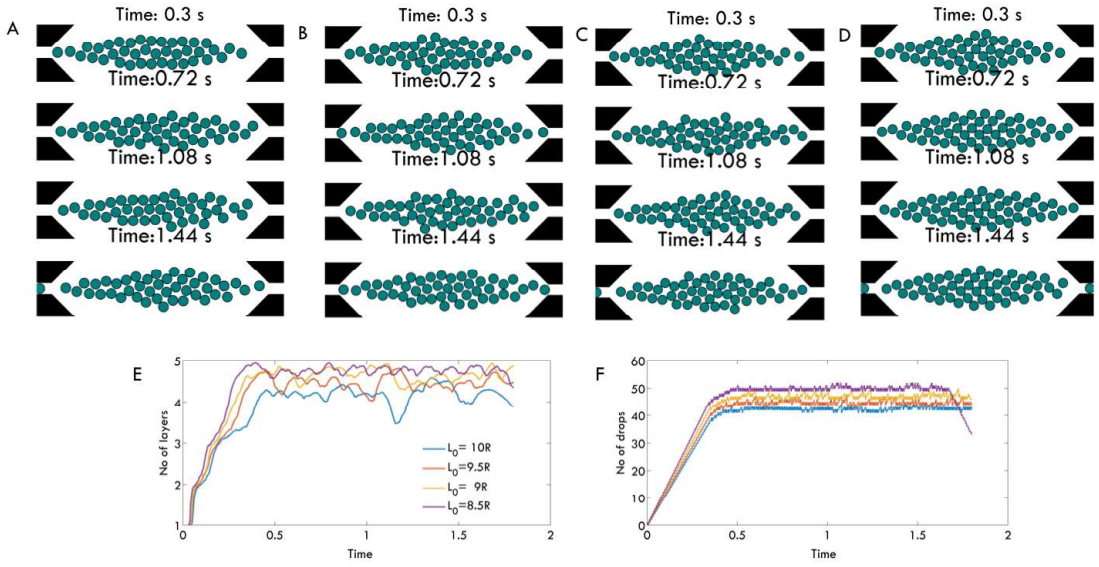

Figure 3-12 Multiple layered configurations for various inlet spacing of drops given by, A) $L_0 \sim 10\ R$; B) $L_0 \sim 9.5\ R$; C) $L_0 \sim 9\ R$; D) $L_0 \sim 8.5\ R$; E) Layers formed inside the channel as a function of time; F) Number of drops in the channel as a function of time. [videos enclosed in CD]

3.3.6 Multiple-layer configurations

When the initial spacing between the drops is reduced even further, drops form multiple layered arrangements inside the channel as shown in Figure 3-12. The three-layer arrangement is no longer able to house the incoming drops, which results in further layering that leads to the increase in the number of layers in the channel. One can estimate the number of layers in the system by calculating the spread of drops in the lateral direction (y-direction), as shown in Figure 3-12 (E). In our simulations we do not get a stable layered configuration which has an integral number of layers greater than three. The drops dynamically self-organize to form ordered arrangements for short periods of time, following which the assembly becomes disordered. The time evolution of layer formation, presented in Figure 3-12 E, shows the formation of a single layer of drops that eventually undergoes layering instability to result in the steep rise to the two-layer configuration. The plot plateaus a little near the two-layer regime, and once this configuration is no longer stable, the system transitions to a three-layer configuration which again becomes unstable resulting in configurations that lie in-between four and five layers. In this regime, drops self-organize to form ordered arrangements, for a short period of time, in the channel as seen in Figure 3-12 A (0.72 s) B(0.72 s) C(1.08 s). We observed, an ordered stable arrangement in the channel when our operating condition was $L_0 \sim 8.5R$. Though the number of layers was between four and five, a periodic spatial pattern was observed as

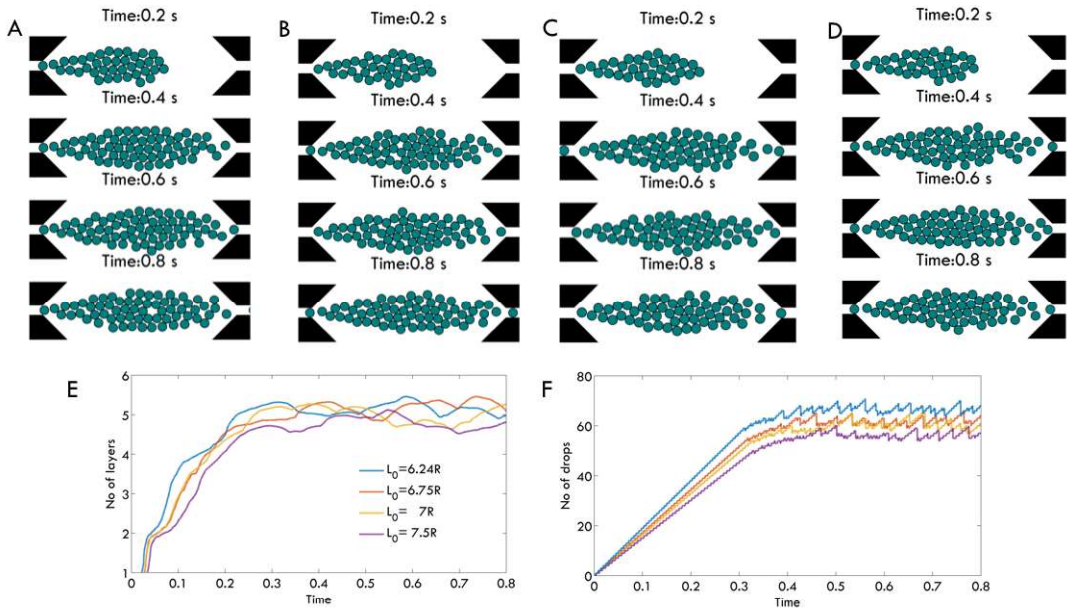

Figure 3-13 Disordered ensemble of drops formed dynamically for various inlet spacing of drops given by, A) $L_0 \sim 6.24\ R$; B) $L_0 \sim 6.75\ R$; C) $L_0 \sim 7\ R$; D) $L_0 \sim 7.5\ R$; E) Layers formed inside the channel as a function of time; F) Number of drops in the channel as a function of time. [videos enclosed in CD]

shown in Figure 3-12 (D). It is interesting to note that the drops arrange in a square lattice instead of a closely packed hexagonal configuration; drops in the central region of the assembly have a maximum of four neighbor drops. Jose and Cubaud[53] reported similar packing of drops in their experiments.

With further reduction in the inlet spacing of drops, the number entering the channel increases which results in the rise in the hold up of drops at steady state as shown in Figure 3-13 (E). At such high hold-ups we observed that drops form disordered arrangements in the channels. Drops often pack tightly; the ones in the central region of the assembly have a maximum of six neighbors. As drops organize, they also dynamically arrange to form ordered assemblies with defects as seen in Figure 3-13 (A- 0.8s, B- 0.4s, C-0.8s). We were able to observe a layered arrangement which approximately had six layers, when the operating condition was $L_0 \sim 6R$, as shown in Figure 3-14. However, the ordered arrangement was not a perfect six layer as reported by Jose and Cubaud[53] (compare Figure 3-14 A with D). This may either be due to the simplistic description for the y-direction force on the drop- due to the flow of continuous phase, the piecewise nature of the drop-drop interaction force- which perturbs the assembly continuously as drops enter at high frequencies, or due to the uncertainty in the correlations for the operating conditions

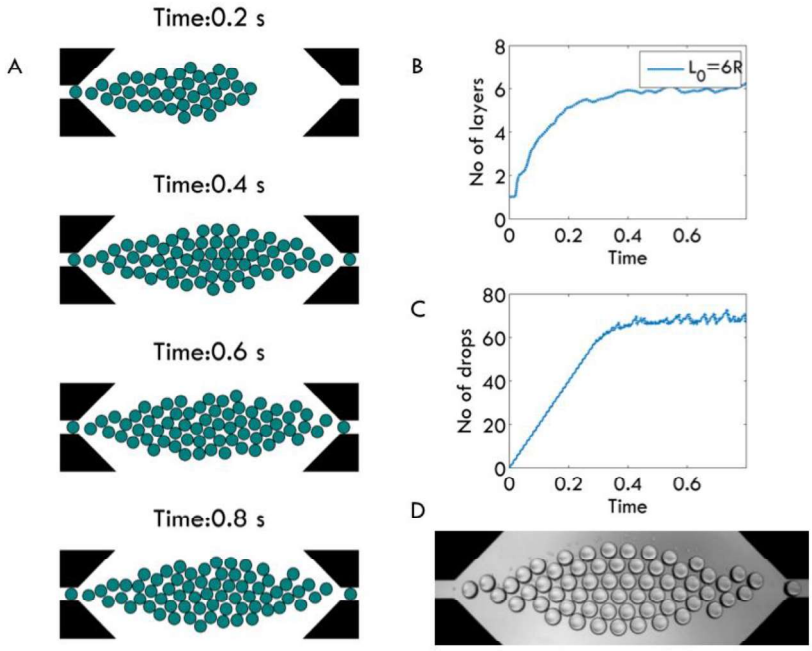

Figure 3-14 Six layered arrangement: A) dynamic pattern formation when $L_0 \sim 6$; B) Layers in the channel as a function of time; C) Hold-up of drops in the channel as a function of time; D) dynamic pattern in the experiments of Jose and Cubaud[53] for $L_0 \sim 6R$. [video enclosed in CD]

provided by Jose and Cubaud- which does not allow us to identify the window of operation that would yield the desired pattern.

3.3.7 Dynamics upon flow reversal

One of the consequences of the linear governing equations (Stokes equations for flow) is the time reversal symmetry. In a multi-agent system, the interactions and the relative motion of agents can render the dynamics non-linear and irreversible with respect to time. In our system, equally spaced drops enter the channel and form different patterns. If the system exhibits time/flow reversal symmetry, one would expect the drops to retrace their path and exit the channel to give back the equally spaced initial configuration. In our system, the layering instability breaks the fore-aft symmetry of the dynamic pattern as observed in (Figure 3-8b and Figure 3-9 f and other multi-layered arrangements). With the flow reversed, the drop-assembly will dynamically rearrange to result in a new steady configuration which is a mirror image of the initial steady state structure with the fore-aft asymmetry. Figure 3-15 shows the dynamics of this rearrangement for the two-layer and three-layer cases. The drops are allowed to enter the channel where they form layered arrangements. Once a steady configuration is attained, the direction of flow is reversed. In Figure 3-15, the snapshots corresponding to time~0, marks the point in time when the flow

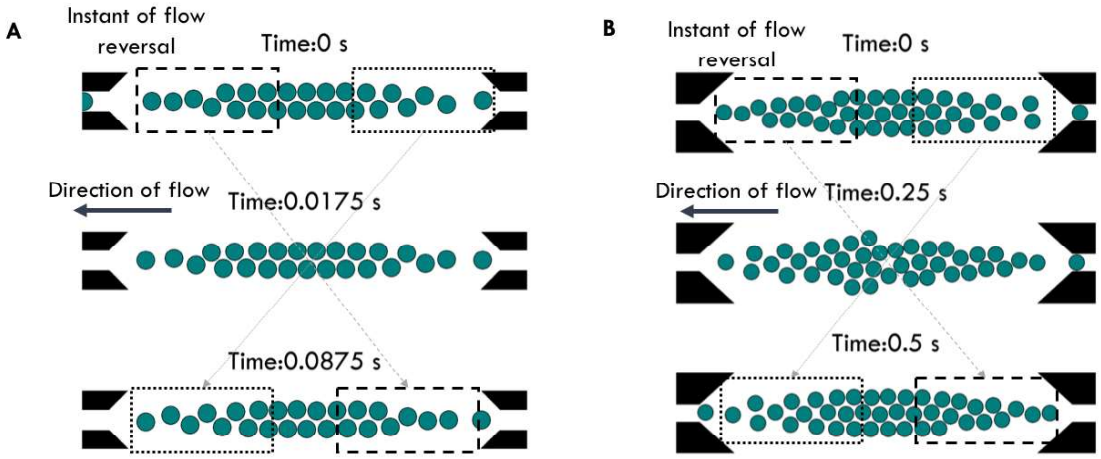

Figure 3-15 Once the drops organize to form a steady state pattern, which corresponds to time=0, the flow direction is reversed: A) Two-layer arrangement $L_0 \sim 18R$; B) Three-layer arrangement $L_0 \sim 12R$. The patterns near the entry and exit, marked by the boxed regions in A and B corresponding to time=0, are interchanged as the flow is reversed. [video enclosed in CD]

is reversed. Now the drops as they exit, rearrange due to the asymmetry in the entry and exit dynamics to form the new steady state configuration (Figure 3-15: A- time~0.0875s and B- time~0.5s), which is a mirror image of the steady state configuration at time~0. Hence the drops will not retrace their path during flow reversal to reach its initial configuration rendering the dynamics irreversible- which implies the absence of time reversal symmetry. This is in fact the reason why the interacting drop traffic models are able to capture the dynamics of the system only after suitable modifications, to the models as shown in Eq(3-13) and (3-14), which break the symmetric nature of the drop-drop and drop-boundary interactions respectively. It is interesting to note that, in the two-layer configuration when drops rearrange, they form an intermediate configuration which has fore-aft symmetry for a short period of time. Also the time scales associated with this re-arrangement strongly depends on the nature of the drop-assembly. The transition in the case of the two-layer arrangement happens in approximately 0.0875 s while for the three-layer case it takes about half a second.

3.3.8 Quantitative characterization

The minimum distance between drops, for a given operating condition, is estimated. It is found to be in good agreement with the experimental results as shown in [Figure 3-16a]. A comparison of the velocities of the drops inside the microchannel, normalized with respect to the velocity in the inlet 1D channel, with the experimental results is showed in Figure 3-16b. The multi-agent simulation was able to predict the trend in the velocity profiles which was similar to the superficial velocity profiles for the channel geometry as

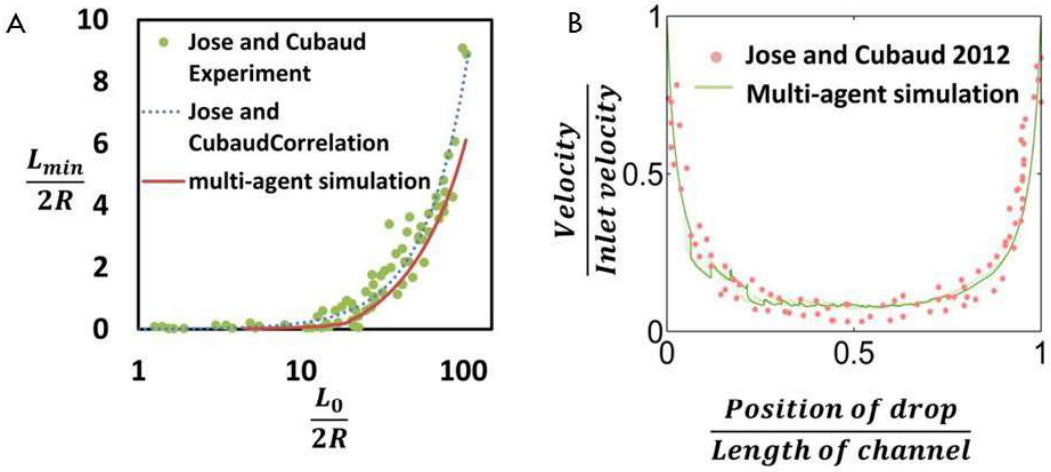

Figure 3-16: A) The minimum distance between two drops inside a microchannel as a function of the inlet spacing: comparison between the experimental results and empirical correlation[53] with the Multi-agent simulation; B) velocity of drops as a function of its position in the channel: comparison between the experimental results [53] with the Multi-agent simulations. [Experimental data was digitized from Jose and Cubaud 2012];

experimentally observed by Jose and Cubaud[53]. The fluctuations in the velocity profiles can be attributed to the piecewise nature of the functional forms Eq (3-6) and (3-7).

3.4 EFFECT OF GEOMETRY IN PATTERN FORMATION

The multi-agent simulation establishes the connection between the rich patterns formed by the drops and the geometry of the microchannel. One of the important insights gained, even with the drop-drop interactions, the velocity of the drops lies in the neighborhood of the superficial velocities [Figure 3-16b]. This fact helps us to understand pattern formation qualitatively. One might be interested in understanding the characteristic features of the microchannel that was responsible in the formation of the rich patterns. From Figure 3-16b, it is clear that we can approximate the velocity field inside the microchannel as a combination of linear decrease of velocity with length at the entrance, flat low velocity mid-region and a linear increase of velocity near the exit. The deceleration field near the diverging entrance and low velocity in a large part of the mid-section are the two characteristic features of the superficial velocity of the microchannel under study (rectangular) that we believe influences the pattern formation. To address this issue, we investigate the dynamics of drops in four different channels. All the four microchannels considered have the same minimum and maximum width of the channel (in the y direction) as that of the rectangular channel. This ensured that the inlet and the minimum superficial velocities were identical. The initial spacing between drops that were used to compare the

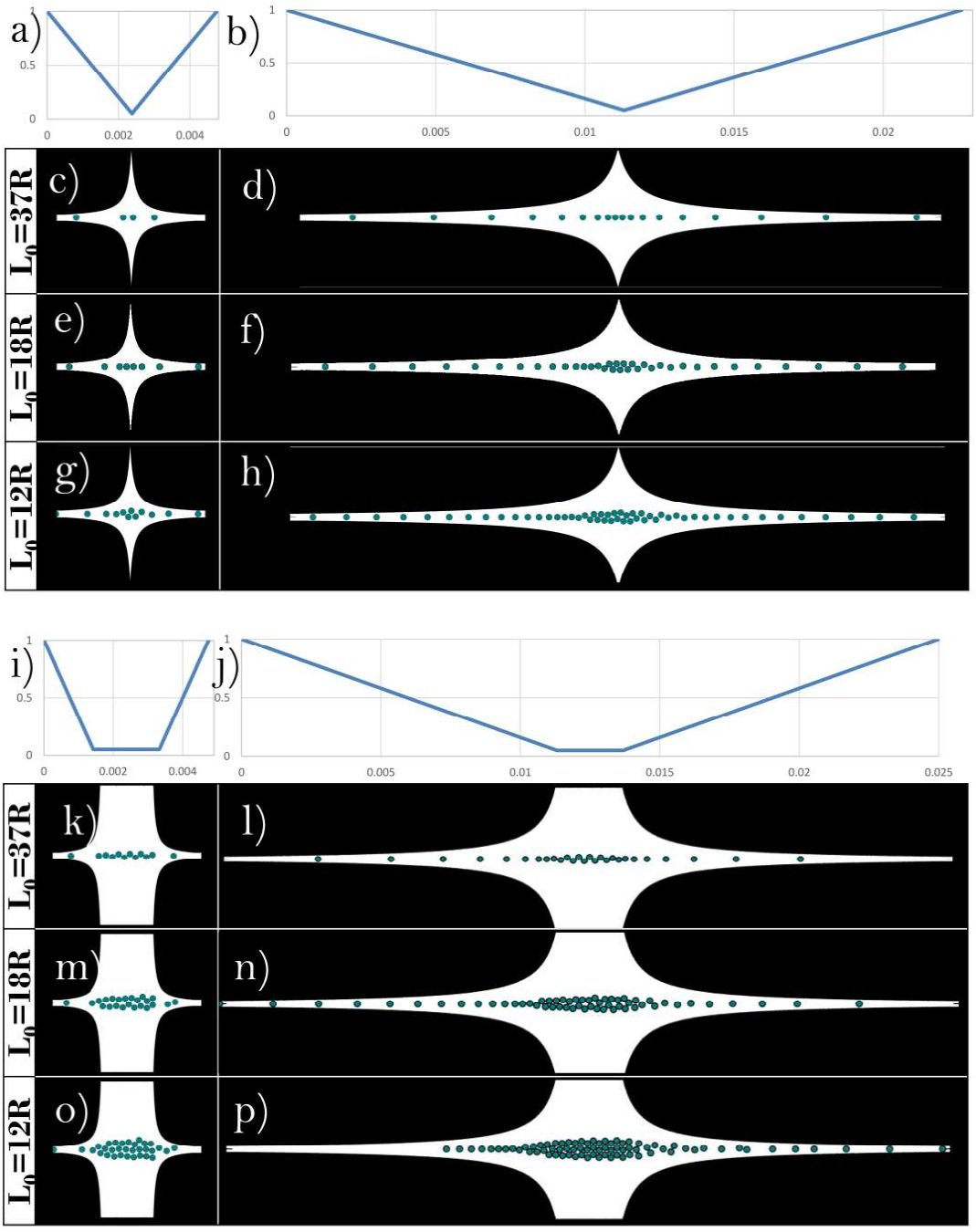

Figure 3-17: (a) velocity profile of microchannel-1 (c), (e), (g); (b) velocity profiles of microchannel-2 (d), (f), (h); (c)-(h): Microchannels with superficial velocities linearly decreasing in the diverging section and linearly increasing in the converging section; (i) velocity profile of microchannel-3 (k), (m), (o); (j) velocity profiles of microchannel-4 (l), (n), (p); (k)-(p) Microchannels with linearly decreasing superficial velocity in the diverging section followed by a region of constant velocity followed by a linearly increasing superficial velocity in the converging section [videos enclosed in CD]

dynamics, were the same as the ones that gave one($L_0 = 37R$), two ($L_0 = 18R$) and three ($L_0 = 12R$) layer configurations for the rectangular microchannel.

First we consider *Microchannel-1*, with superficial velocity fields, linearly decreasing and increasing along the length [Figure 3-17 a]. From Figure 3-17 c, e, g one can observe that

the drops did not layer as expected. Now the next question would be to find out the features of the microchannel that will result in pattern formation. This encouraged us to design *Microchannel-2* in which the length of the diverging section is increased [Figure 3-17 b, d, f and h]. We can observe from Figure 3-17 d, f, h that the drops layered as expected and could form one and two layers and two layers becoming unstable. In comparison with the Microchannel-1, the rate at which the superficial velocity decreased along the length of Microchannel-2 is lower. This feature of the microchannel aids in the formation of layered arrangements. Deceleration of drops in microchannel-2 is lower than 1 but the time spent by drops in the diverging section is higher in 2 than in 1. Because the drop feeding rate is kept constant for both the microchannels, the number of drops in the diverging section of microchannel-2 is greater than that of 1. This results in more crowding of drops and aids in the formation of layered configurations.

Microchannel-3 is designed to understand the effect of the low-flat-velocity mid-section in the microchannel [Figure 3-17 i]. From Figure 3-17 k, m and o, it is clear that the patterns formed are close to one, two and three layers. This is the result of the similarity between microchannel-3 and the rectangular microchannel because the velocity profile of 3 [Figure 3-17 i] captures features of the velocity profile of the rectangular microchannel [Figure 3-16 b]. Dynamics of drops in microchannel-2 helps us to understand the role of a slowly diverging section of a microchannel in pattern formation. Hence *microchannel-4* was designed with an intent to understand the combined effect of the slow deceleration and flat velocity sections of the microchannel [Figure 3-17 j]. From Figure 3-17 l, n and p, one can conclude that the qualitative features of the patterns formed are the same as microchannel-3. The increased number of drops and close packing of drops in the patterns formed in microchannel-4 are due to the excessive crowding of drops in the slow diverging sections. It becomes clear from the above analysis that the low-flat velocity mid-section of the microchannel has a greater effect on pattern formation than the decelerating field from the diverging section of the microchannel. This is the reason for the rich patterns observed by Jose and Cubaud[53] in their rectangular geometry.

3.5 DROPS AND VEHICULAR TRAFFIC

Traffic of vehicles is not very different from that of drops in microchannels. Our experience with driving has helped in understanding the similarities and differences between the two seemingly different phenomena. Let's consider the case where there are

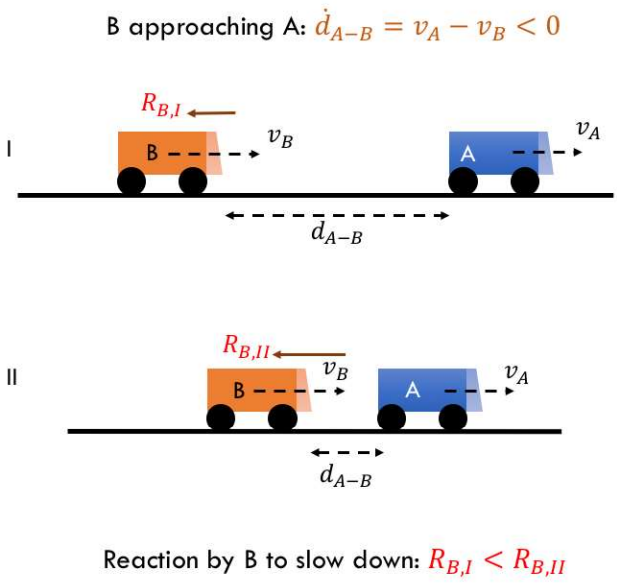

Figure 3-18 Two vehicles A and B which are spaced apart are approaching each other at a rate equal to. I and II correspond to scenarios where the vehicles at a particular instant of time are spaced apart differently. The reaction of vehicle B to slow down would be higher for case II where the vehicles are closer to each other compared to case I.

two drivers, A and B, with B behind A separated by an instantaneous distance d_{A-B}, on a straight line moving in the same direction. When A slows down, either because the destination is near or to take a turn, B will also slow down to avoid impending collision. This changes the distance between the vehicles which results in non-zero $\dot{d}_{A-B}$: when $\dot{d}_{A-B} < 0$ A and B approach each other. Now the dynamic response of B to the slowing down of A, is dependent on the rate of approach $\dot{d}_{A-B}$ and relative distance d_{A-B}. When A and B are very far from each other ($d_{A-B} > d_{cr}$), B may not be affected by the change in the relative distance d_{A-B}. As A and B reach the interacting distance, where $d_{A-B} \leq d_{cr}$, as illustrated in Figure 3-18 (case I), one would expect B to react calmly to the change in the relative distance between A and B. However, when they are very close to each other, the reaction that B exhibits to slow down, would be greater as illustrated in Figure 3-18 (case II). From this scenario, one can easily deduce the $(1/d_{A-B})$ functional dependence of reaction (R_B) of B on d_{A-B}. It is also observed that vehicles can travel together without any reaction from B as long as A and B do not approach each other or move away from each other ($\dot{d}_{A-B} > 0$). One can summarize the above mentioned effects mathematically, as shown in Eq (3-15).

The functional form for the reaction of the trailing vehicle B is observed to be analogous to the drop-drop interaction term described in Eq (3-13). Traffic of drops in a microchnnel

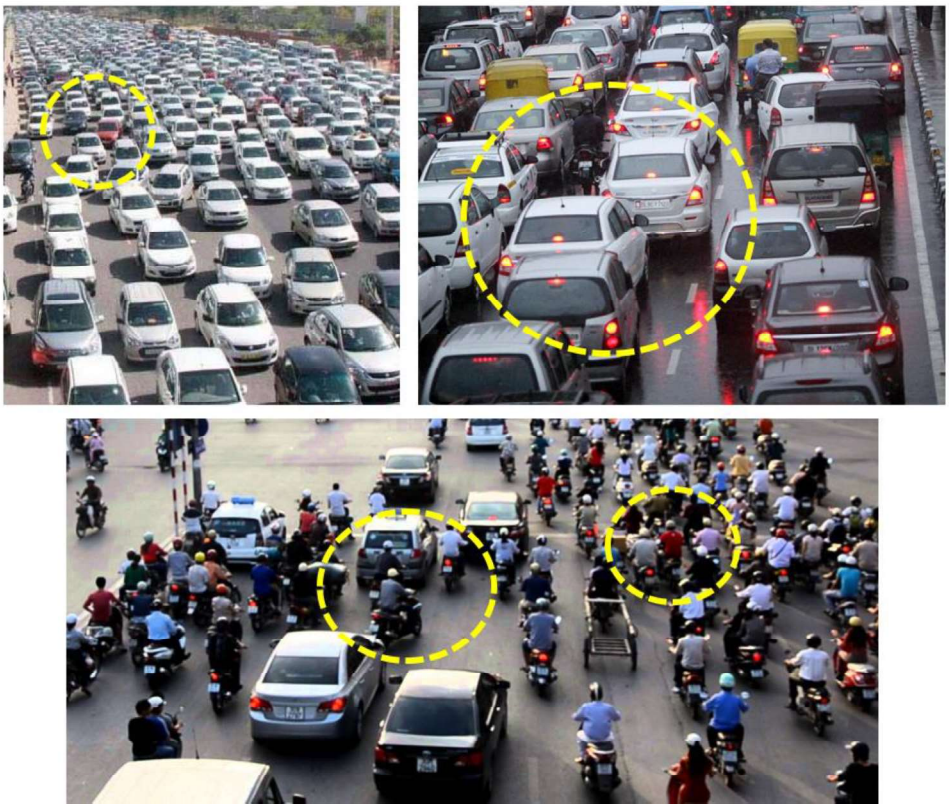

Figure 3-19 Images of Indian traffic (picked from random sources in the Internet) where layering is observed. Drivers in a non-lane road in India often choose to cut lines in an aim to move forward. The regions in the images marked by dashed curves show instances of layering.

is a result of hydrodynamic interactions due to lubrication flow while vehicular traffic is a consequence of human decisions during driving. The length and time scales associated with both the phenomena and the nature of interactions are very different. Yet the mathematical equivalence between the two phenomena is fascinating.

$$R_B = \begin{cases} k_v\left(\dfrac{\dot{d}_{A-B}}{d_{A-B}}\right) & \dot{d}_{A-B} < 0, \;\; d_{A-B} < d_{cr} \\ 0 & elsewhere \end{cases} \qquad (3\text{-}15)$$

Another interesting similiarity is the phenomenon of layering. Drops layer in a microchannel as consequence of crowding. In traffic flow, especially on Indian roads where lane flow is seldom enforced, one can observe vehicles overtaking other vehicles to move ahead as shown in the boxed regions of Figure 3-19. In both cases one can observe common reasons for layering: the inability of the entity to move forward (due to the slow moving preceding drop or vehicle) and the drive to move forward (relative velocities due

to the flow fields of the diverging geometry in the drop-traffic case, wheras it is a driver in a hurry in the vehicular traffic case).

3.6 CONCLUSION

An agent based framework is employed to study the complex, dynamic pattern formation of drops in 2D microchannels with a top-down symmetry. Interacting drop-traffic models are proposed, which are a set of phenomenological models, that approximately quantify the different forces acting on the drops as they flow in the microchannel. These models are then incorporated into a multi-agent simulation which solves the Newton's second law of motion to determine the position and velocity of drops in the channel. The results of the simulation are validated with the experiments of Jose and Cubaud[53] reported in the literature. Though the models used for describing the forces are simple, it is very interesting to observe a quantitative match between our numerical simulations and experiments. The multi-agent simulations capture the dynamic crowding of drops which ultimately leads to a layering instability that results in ordered drop-arrangements. The layered configurations observed by Jose and Cubaud lack fore-aft symmetry due to the absence of time-reversal property. By modifying the interacting drop-traffic models suitably, we are able to capture this asymmetry in the patterns formed. We observe that the velocity of the drops is always in the neighborhood of the superficial velocity corresponding to the microchannel. This allows us to build a set of microchannel geometries to understand qualitatively, that feature in the superficial velocity profile corresponding to the geometry used by Jose and Cubaud[53] that results in the formation of multiple layers.